RSC Advances

PAPER

View Article Online
View Journal | View Issue

Cite this: *RSC Adv.*, 2025, **15**, 43174

Ion transport dynamics and cation mobility in hydrothermally synthesized MXene-$NiWO_4$ composite electrodes for advanced energy storage

Sana Ullah Asif, *[a] Aqsa Nadeem,[b] Savera Bibi,[c] Muhammad Ehsan Mazhar, *[c] Abdul Shakoor,[d] Majed M. Alghamdi,[e] Shahid Atiq, [d] Asma Rasheed,[d] Adel A. El-Zahhar,[e] Farooq Ahmad *[d] and Muhammad Ahmed Khan *[d]

Excessive consumption of fossil fuels over the years has severely impacted the global environment, causing air pollution and climate change. Thereby, developing renewable and efficient energy storage systems has become essential to overcome these challenges. In this context, supercapacitors (SCs) have attracted significant attention due to their rapid charge–discharge performance, higher power density (PD), longer cycle life, and environmental friendliness. In this study, $NiWO_4$/MXene composite electrodes were synthesized *via* a hydrothermal route with the aim of achieving enhanced cation mobility and accelerated ion transport, thereby improving electrochemical efficiency and charge storage performance. The material's electrochemical performance was tested using cyclic voltammetry (CV) for redox behavior and galvanostatic charge–discharge (GCD) for charge storage capacity and stability. The $NiWO_4$/MXene electrode delivered a high specific capacitance of 1545.42 F g^{-1} at a current density of 1.5 A g^{-1}, along with an energy density (ED) of 107.32 Wh kg^{-1} and a PD of 199.9 W kg^{-1}. The chronoamperometry results confirm that the composite exhibits excellent electrochemical stability over 50 hours and 95.80% capacitance retention from GCD after 2000 cycles. A systematic correlation was observed between the structural features such as the reduction in diffraction peak intensity due to MXene coverage and the preservation of $NiWO_4$ crystal planes and the ion transport dynamics, indicating that the structural modulation directly influences cation mobility and overall charge transport. These findings demonstrate that careful tuning of the material's structure can effectively enhance ion transport in composite electrode materials.

Received 3rd October 2025
Accepted 28th October 2025

DOI: 10.1039/d5ra07538f

rsc.li/rsc-advances

1. Introduction

As global populations grow, the need for natural energy resources rises quickly. Currently, fossil fuels contribute to climate change and severely threaten human survival. In this situation, there is an urgent need to find eco-friendly, sustainable, and renewable energy sources.[1–3] As a result, technologies like batteries, fuel cells, and SCs have been developed to meet the increasing demand for energy storage and supply. Electrochemical energy storage (EES) devices and their materials are now essential for solving long-term energy problems. Recent breakthroughs in electrochemical processes have led to high-performance batteries and SCs that provide more power and last longer than traditional models. Since weight and cost limitations in conventional batteries have driven interdisciplinary research, efforts are focused on creating innovative solutions to improve performance, efficiency, and affordability.[4–6]

However, SCs were discovered as an attractive option for electrochemical energy conversion and storage, offering superior benefits such as higher ED than conventional capacitors and higher PD than batteries, with remarkable cycle life and improved performance. Additionally, they have demonstrated greater PD than batteries for powering portable and flexible electronic devices, making them an attractive alternative for next-generation energy storage applications.[7] SCs are generally classified into three categories based on their charge storage mechanisms: electrical double-layer capacitors (EDLCs), which store charge electrostatically at the electrode–electrolyte interface; pseudocapacitors (PCs), which store charge through fast and reversible Faradaic redox reactions at or near the electrode surface; and battery-type capacitors, which store charge *via*

[a]*Department of Physics, Qilu Institute of Technology, Jinan 250200, Shandong, P. R. China. E-mail: sanaullahasif@gmail.com*
[b]*Department of Physics, Lahore College for Women University, Lahore, Pakistan*
[c]*Institute of Physics, Bahauddin Zakariya University Multan, Pakistan. E-mail: dr.ehsan@bzu.edu.pk*
[d]*Centre of Excellence in Solid State Physics University of the Punjab, Lahore, Pakistan. E-mail: amykhan.931@gmail.com*
[e]*Department of Chemistry, College of Science, King Khalid University, P.O. Box 9004, Abha 61413, Saudi Arabia*

slower bulk Faradaic reactions involving ion intercalation.[8,9] The $NiWO_4$/MXene composite studied here primarily exhibits pseudocapacitive behavior, driven by the rapid redox reactions of $NiWO_4$ and the EDLC contribution from MXene.

To enhance the energy storage capabilities of SCs, researchers focus on several key strategies: developing innovative electrode materials and elevating cell voltage. Two prominent approaches have emerged to achieve these enhancements: using organic electrolytes and designing asymmetric SCs, both of which offer promising pathways to optimize SC performance.[10] SCs use a variety of electroactive materials, including conducting polymers, metal oxides (MOs), and carbon, among others.[11] Nanostructured inorganic compounds, particularly transition metal oxides (TMOs) and their derived substances using elements such as Mn, Ca, Ni, W, Fe, and Zn, have become highly promising for energy storage devices because of their outstanding aspects, including a greater surface area, more excellent stability, and outstanding electrical properties.[12]

Transition-metal tungstates are of interest because they exhibit unique physical, chemical, and energy-storage properties.[13] Transition metal tungstate typically follows the chemical formula AWO_4, in which A represents a divalent cation (A^{2+}) that functions as a network modulator.[14] Nonetheless, bivalent cations like nickel functions effectively in SCs due to their lower ionic radii (less than 0.77 Å). In contrast to other substances, tungsten dioxide and related metal tungstates offer several advantages, including safe and inexpensive production, extreme resistance to ultraviolet radiation, and adaptability.[15] Furthermore, metal tungstates are bimetallic compounds that offer superior energy storage capabilities compared to monometallic compounds such as NiO and WO_3. Among these tungstates, $NiWO_4$, $CoWO_4$, and Bi_2WO_6 have garnered significant attention due to their outstanding faradaic activities, which enable enhanced energy storage capacities, and these qualities make them viable choices for energy conservation applications.[16] Notably, Ni–O and $NiWO_4$ have distinct electrochemical characteristics, are ecologically harmless, and have better specific capacitance (C_{sp}).[17] However, single-metal tungstates have significant drawbacks, including low energy storage capacity, poor high-speed performance, and a short lifespan.[18–21]

To address the limitations of pure $NiWO_4$, various carbon-based materials, including activated carbon (AC), graphene oxide (GO), carbon nanotubes (CNTs), and MXene, have been investigated. Among these, MXene features a 2D layered structure with high electrical conductivity, a large surface area, strong stability, magnetic properties, and durability.[19] Notably, combining MXenes with MOs has shown significant improvements in electrochemical performance. Moreover, the interplay between structural features and ion-transport dynamics is pivotal for optimizing the performance of nanomaterial-based composites. Recent studies have shown that incorporating nanomaterials can significantly alter ion-conduction pathways. For instance, the arrangement of polymer chains and the presence of inorganic fillers can impact ion transport properties. Research by Choi *et al.*[22] demonstrated that the medium's structural characteristics influence ion mobility in confined spaces. Additionally, a review by Gerdroodbar *et al.* elucidated the intricate interplay between ions, solvents, salts, and the electrolyte matrix, emphasizing the importance of structural considerations in ion transport.[23]

Although significant progress has been made in developing advanced electrode materials for SCs, a major knowledge gap persists in correlating ionic transport phenomena—including ionic conductivity, diffusion kinetics, and cation mobility—with the ultimate electrochemical performance. Most reported studies emphasize composition or morphology optimization, while overlooking the fundamental ion–electron coupling mechanisms that dictate real device efficiency. Herein, we present a rationally engineered $NiWO_4$/MXene composite that demonstrates not only high active surface availability and rapid electron pathways but also markedly enhanced ion mobility and diffusion dynamics, enabling faster charge transport across the electrode–electrolyte interface. By systematically probing the structure–transport–performance relationship, this work reveals how ionic motion contributes to superior capacitance and rate capability. The novelty of our study lies in unifying material design with deep transport property investigation, providing new scientific insights that guide the development of next-generation SCs with high PD and long-term stability.

2. Experimental section

2.1. Materials

In the preparation of sample $NiWO_4$ and $NiWO_4$/MXene, chemicals used include nickel nitrate hexahydrate ($Ni(NO_3)_2 \cdot 6H_2O$) purchased from Irritant, sodium tungstate dihydrate ($Na_2WO_4 \cdot 2H_2O$) from Thomas Baker, potassium hydroxide (KOH) from Duksan, and additional MXene chemicals were also used. Analytical-grade substances were used throughout production, and no further purification was required.

2.2. Synthesis of MXene

Ti_3AlC_2 MAX powder (0.1 g) and KOH (0.35 g) were ground for 2 hours, with 2.5 mL of deionized water (DIW) added dropwise during grinding, yielding a thick, jelly-like paste. The paste was then transferred to a Teflon-coated stainless-steel autoclave and heated at 180 °C for 24 hours. After hydrothermal synthesis, the sample was washed with DIW and ethanol, maintaining a pH of 6–7. The washing process exfoliated the MXene layers, which were then separated by centrifugation and dried at 60 °C for 12 hours.

2.3. Synthesis of $NiWO_4$

A typical procedure, the hydrothermal method, was used to produce nickel tungstate ($NiWO_4$): 60 mL of DIW was used to dissolve 5.23 g of Ni $(NO_3)_2 \cdot 6H_2O$ and 7.3 g of $Na_2WO_4 \cdot 6H_2O$. The mixture was stirred continuously for 50 minutes at room temperature, yielding a greenish-colored solution with a few precipitates. The colored solution was made transparent by adding dropwise KOH solution (to maintain a pH of 10). The resulting solution was transferred to a 100 mL Teflon-lined

autoclave and heated to 160 °C for 4 hours. After an 8-hour rest and subsequent cooling, the samples were collected and transferred into washed and filtered centrifuge tubes. The samples were rinsed three times with DIW and once with ethanol to remove contaminants. After drying at 80 °C, the material was ground into a fine powder using a mortar and pestle. Finally, the powder was annealed at 450 °C for 4 hours. The finished product was stored in an Eppendorf tube for characterization.

2.4. Preparation of $NiWO_4$/MXene

The $NiWO_4$/MXene composite (75 : 25 wt%) was prepared by dispersing 150 mg of $NiWO_4$ and 50 mg of MXene into 60 mL of DIW under continuous magnetic stirring for 50 minutes. Then, the material was transferred to an autoclave at 160 °C for 4 hours. After that, the material was taken out and cooled to ambient temperature. It was then centrifuged three times with DIW and ethanol to remove impurities; finally, the sample was transferred to a Petri dish and dried at 80 °C. Subsequently, the material was ground into a powder and stored for further analysis.

2.5. Fabrication of the working electrode

For the fabrication of the working electrode (WE), nickel foam (NF) was cut into small sections measuring 1.5 × 1.5 cm^2 and cleaned *via* ultrasonication with ethanol, HCl (10%), and distilled water. Afterward, NF was dried in a thermal oven at 50 °C for 30 minutes. To prepare the electrode ink, 0.012 g of active material ($NiWO_4$/MXene), 0.0015 g of carbon black, and 0.0015 g of PVDF were mixed with 75 μL of NMP solvent (*N*,*N*-dimethylformamide). After mixing for 1 hour, the catalytic ink was drop-cast onto the NF. Following deposition, the functional (active) material was dried in an oven at 70 °C for 24 hours. The active material loading for WE fabrication was 2 mg. Before electrochemical testing, the Pyrex glass cell was thoroughly cleaned with ethanol and distilled water to remove contaminants. All electrodes were prepared using the same protocol, and the WE was used to investigate the electrochemical characteristics of SCs. The procedure for synthesizing the $NiWO_4$/MXene nanomaterial and fabricating the electrode is illustrated in Fig. 1.

2.6. Materials characterizations

XRD analysis was used to determine the crystalline structure of pure $NiWO_4$ and composite $NiWO_4$/MXene (Bruker D8 Phaser). High-resolution surface topography images were obtained using a field-emission scanning electron microscope (FEI Nova 450 Nano SEM). Elemental analysis was performed using an EDX instrument from Oxford Instruments. Chemical composition analysis of the materials was conducted using XPS on the Thermo Fisher Nexsa-XPS system (Queen Mary University of London, UK). Electrochemical measurements were performed using a Corrtest CHI 660 with an Ag/AgCl reference electrode, a $NiWO_4$ or $NiWO_4$/MXene working electrode, and a platinum wire as the counter electrode in 3 M KOH.

Subsequent eqn (1) was utilized to calculate C_{sp} employing the cyclic voltammetry curve:[24–26]

$$C_{sp} = \frac{\int i(V)\mathrm{d}V}{mVS}\left(\mathrm{F\ g^{-1}}\right) \quad (1)$$

where $\int i(V)\mathrm{d}V$ represents the area under the curve, m denotes the mass of active material (2 mg) on the electrode, V signifies the voltage window (V), and S indicates the sweep rate (mV s^{-1}).

Eqn (2) was utilized to determine C_{sp} using the galvanostatic charge–discharge curve:[27]

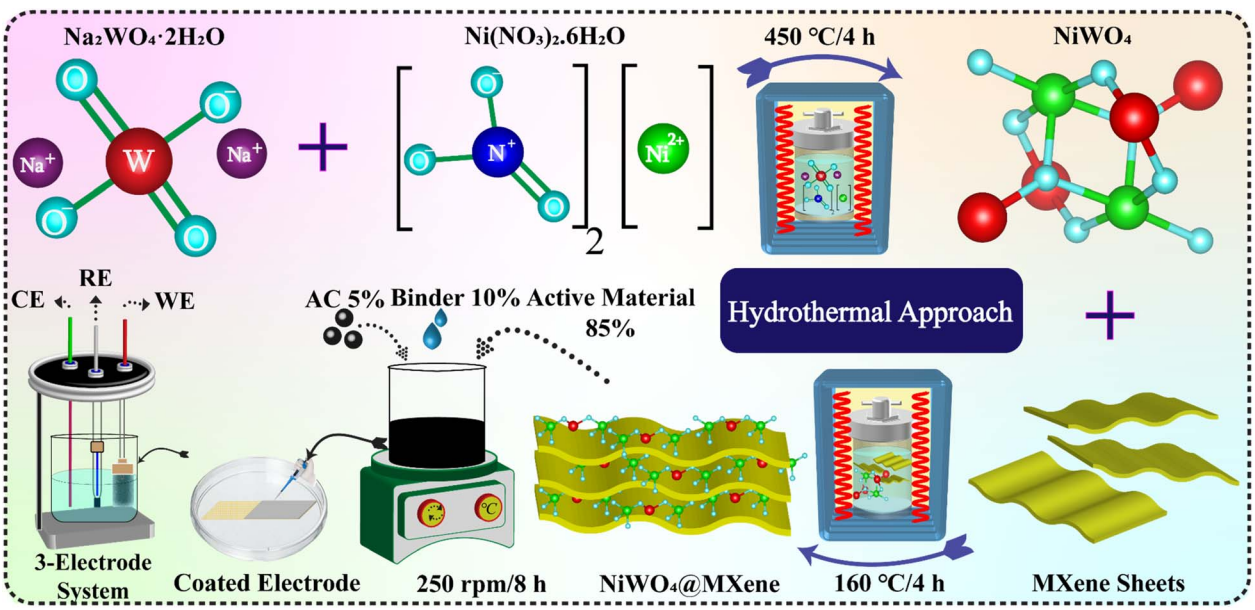

Fig. 1 Schematic profile of sample synthesis.

$$C_{sp} = \frac{I \times \Delta t}{m \times \Delta V} (\mathrm{F\ g^{-1}}) \quad (2)$$

Here, I represents current (A), Δt denotes discharge duration, m signifies mass of active material, and ΔV indicates potential difference.

ED is measured in terms of Wh kg^{-1} from eqn (3):[28,29]

$$\mathrm{ED} = \frac{1}{2} \frac{C_{sp} \times \Delta V^2}{3.6} (\mathrm{Wh\ kg^{-1}}) \quad (3)$$

Here, PD is measured by eqn (4):[28]

$$\mathrm{PD} = \frac{\mathrm{ED} \times 3600}{\Delta t} (\mathrm{W\ kg^{-1}}) \quad (4)$$

3. Results and discussion

3.1. Structural analysis

The structural analysis of the materials was performed using X-ray diffraction (XRD). The XRD patterns of pure $NiWO_4$ and the $NiWO_4$/MXene composite are presented in Fig. 2(a), confirming the crystalline phases of the samples. Samples were scanned over a range from 10° to 80°. The peaks in each diffraction pattern for pure $NiWO_4$ are observed at 2θ = 15.61°, 19.28°, 23.96°, 24.92°, 30.92°, 31.21°, 36.57°, 39.11°, 41.66°, 44.74°, 46.40°, 49.04°, 51.43°, 52.32°, 54.62°, 62.34°, 65.52°, 68.94°, and 72.37°, corresponding to the lattice planes (010), (100), (011), (110), ($\bar{1}$11), (020), (002), (200), ($\bar{1}$02), ($\bar{1}$12), ($\bar{2}$11), (022), (220), (130), ($\bar{2}$02), ($\bar{1}$13), ($\bar{3}$11), (041), and ($\bar{1}$41), respectively. All observed diffraction peaks can be indexed to monoclinic $NiWO_4$ and match well with JCPDS card No. 00-015-0755. The main reason for the reduction in the diffraction peak intensity is the coverage of the $NiWO_4$ basal planes with MXene nanosheets. Therefore, the MXene peaks appear at 19.1°, corresponding to the *hkl* value (004), and another peak at 35.63°, aligned with the (111) crystal plane, as indexed in JCPDS card no. 00-032-1383. Additionally, the successful synthesis of the $NiWO_4$/MXene nanocomposite is confirmed by the presence of both $NiWO_4$ and MXene phases, as evidenced by their respective peaks. The absence of additional peaks in $NiWO_4$/MXene indicates the material's high purity. The reduction in the intensity of all diffraction peaks is due to the growth of MXene nanosheets on $NiWO_4$. Furthermore, the crystal structure of $NiWO_4$ was modeled using VESTA software and is displayed in Fig. 2(c). Rietveld refinement was performed to confirm the crystal structure and phase purity of the sample. The refinement pattern of the parent sample ($NiWO_4$) is shown in Fig. 2(b).

3.2. X-ray photoelectron spectroscopy (XPS) analysis

XPS was used to examine the oxidation states and surface chemical bonding of the $NiWO_4$ and $NiWO_4$/MXene specimens, as shown in Fig. 3(a–f). The XPS spectrum overview, as seen in Fig. 3(a), confirms the presence of W, Ni, and O based on their characteristic binding energies. High-resolution spectra for Ni 2p, W 4f, O 1s, C 1s, and Ti 2p are shown in Fig. 3(b–f). As shown in Fig. 3(b), the Ni 2p spectrum features doublet states of Ni $2p_{1/2}$ and Ni $2p_{3/2}$ at binding energies of 873.1 and 855.8 eV, respectively, along with two satellite peaks, indicating that Ni is mainly in the +2 oxidation state.[16] Fig. 3(c) presents a detailed XPS analysis of W 4f, showing a spin–orbit doublet with W $4f_{5/2}$ at 37.42 eV and W $4f_{7/2}$ at 35.02 eV, indicating that W exists in the +6 oxidation state in the synthesized material. In Fig. 3(d), the primary O 1s XPS spectrum of the $NiWO_4$/MXene hybrid showed two dominant peaks. The peak at 530 eV corresponds to metal–oxygen linkages (M–O), related to Ni–O and W–O bonds in $NiWO_4$, as well as Ti–O bonds in the MXene. The secondary peak at 531 eV is associated with oxygen deficiencies, surface imperfections in $NiWO_4$, and hydroxyl (–OH) groups on the MXene surface. This dual assignment highlights the synergistic contributions from both components in the hybrid. The C 1s spectrum in Fig. 3(e) shows that carbon, characterized by a peak at 285.6 eV, is associated with the MXene. The detailed Ti 2p XPS spectrum (shown in Fig. 3(f)) can be deconvoluted into Ti $2p_{3/2}$ and Ti $2p_{1/2}$ peaks. The Ti $2p_{3/2}$ peak appears at 454.2 eV, indicating titanium–carbon (Ti–C) bonds, while a` peak at 459.2 eV corresponds to titanium dioxide (TiO_2).

3.3. Morphological analysis

The surface topography of synthesized materials was analyzed using FESEM. Fig. 4(a) shows that $NiWO_4$ has a dense, highly clustered granular structure made up of irregular micrograins.

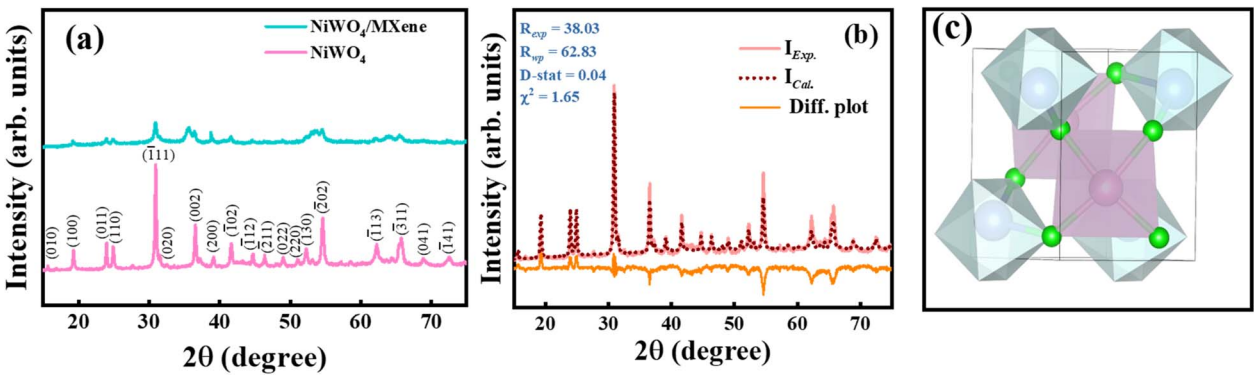

Fig. 2 (a) XRD spectra of $NiWO_4$ and $NiWO_4$/MXene, and (b) Rietveld refinement pattern of $NiWO_4$ and (b) crystal structure of $NiWO_4$.

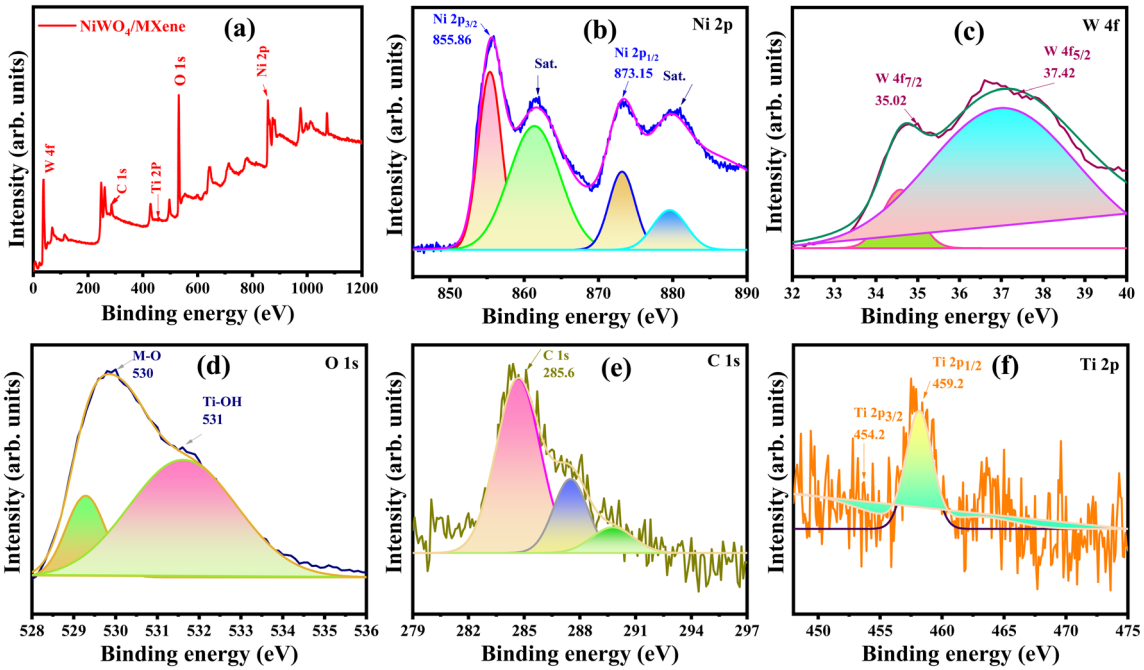

Fig. 3 (a) Survey spectra of $NiWO_4$/MXene, (b) survey spectra of Ni, (c) W, (d) O, (e) C, and (f) Ti.

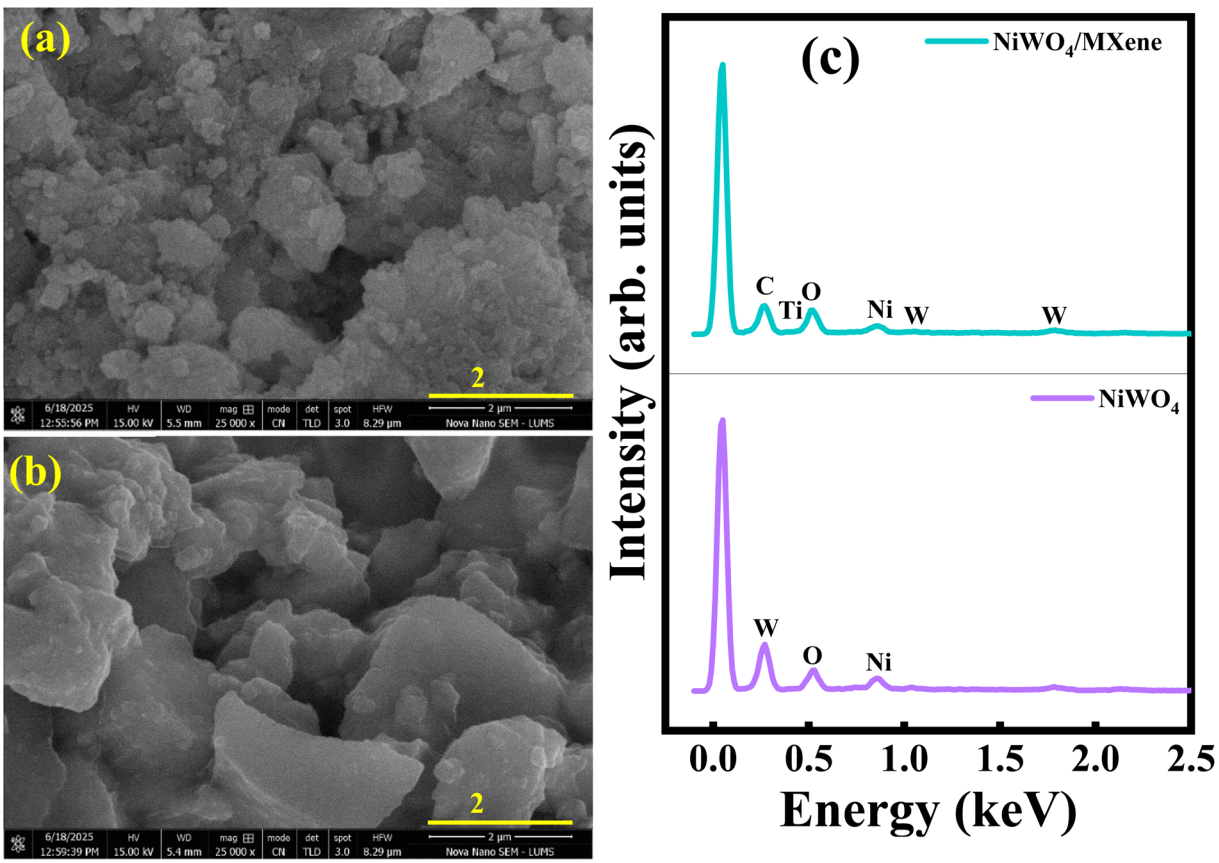

Fig. 4 (a) FESEM image of $NiWO_4$, (b) $NiWO_4$/MXene, and (c) EDX spectra of both samples.

Table 1 Elemental composition of $NiWO_4$ and $NiWO_4$/MXene

Sample	Wt% (Ni)	Wt% (W)	Wt% (O)	Wt% (Ti)	Wt% (C)
$NiWO_4$	23	71	6	0	0
$NiWO_4$/MXene	18	58	5	15	4

This agglomeration may occur due to the surface energy inherent to nanomaterials. In contrast, Fig. 4(b) displays the FESEM image of the $NiWO_4$/MXene composite, revealing a significant change in morphology. The $NiWO_4$ particles appear to be dispersed over wrinkled, layered MXene sheets, indicating effective integration. The layered structure of MXene provides a large surface area and serves as a supporting framework to prevent $NiWO_4$ particle agglomeration, thereby enabling more accessible active sites and enhancing electrochemical performance. EDX spectra further verify the successful synthesis of both samples. Fig. 4(c) confirms the presence of W, Ni, and O in pure $NiWO_4$, with peaks of Ni, W, O, and distinct signals of Ti and C, corresponding to elements from MXene. The composition of the prepared samples is displayed in Table 1.

EDX analysis with elemental mapping (Fig. 5) was used to examine the elemental composition and spatial distribution within the $NiWO_4$/MXene composite. Mapping results confirmed the consistent presence of W, Ni, O, C, and Ti elements across the sample, verifying the successful integration of $NiWO_4$ onto the MXene matrix. The even distribution of these elements indicates strong interfacial interaction between $NiWO_4$ nanostructures and conductive MXene sheets. This uniformity is essential for ensuring efficient charge transport and improved electrochemical performance. Additionally, the absence of any extra elemental peaks confirms the chemical purity and successful fabrication of the $NiWO_4$/MXene composite.

3.4. Electrochemical analysis

The charge storage capabilities of $NiWO_4$ and $NiWO_4$/MXene were evaluated using CV, GCD, and electrochemical impedance spectroscopy (EIS) in 3 M potassium hydroxide (KOH) aqueous solution, with a three-electrode setup. The charge storage abilities of $NiWO_4$ and $NiWO_4$/MXene electrodes were assessed from their CV curves (Fig. 6(a–c)) at various scan rates (5 to 40 mV s^{-1}) within the −0.05 to 0.65 V range. The CV curves exhibit redox peaks, indicating electrochemical reactions at the electrode surface driven by electron transfer between the electrode and the electrolyte. As the scan rate increases, anodic peaks (oxidation) tend to shift toward higher potentials due to increased internal resistance, kinetic limitations, or mass transport issues, while cathodic peaks (reduction) shift toward lower potentials. Additionally, the current response increases with scan rate, resulting in a larger area under the CV curve, indicating enhanced charge storage capacity and electrochemical activity through faster charging/discharging and greater electrochemical engagement. This behavior provides

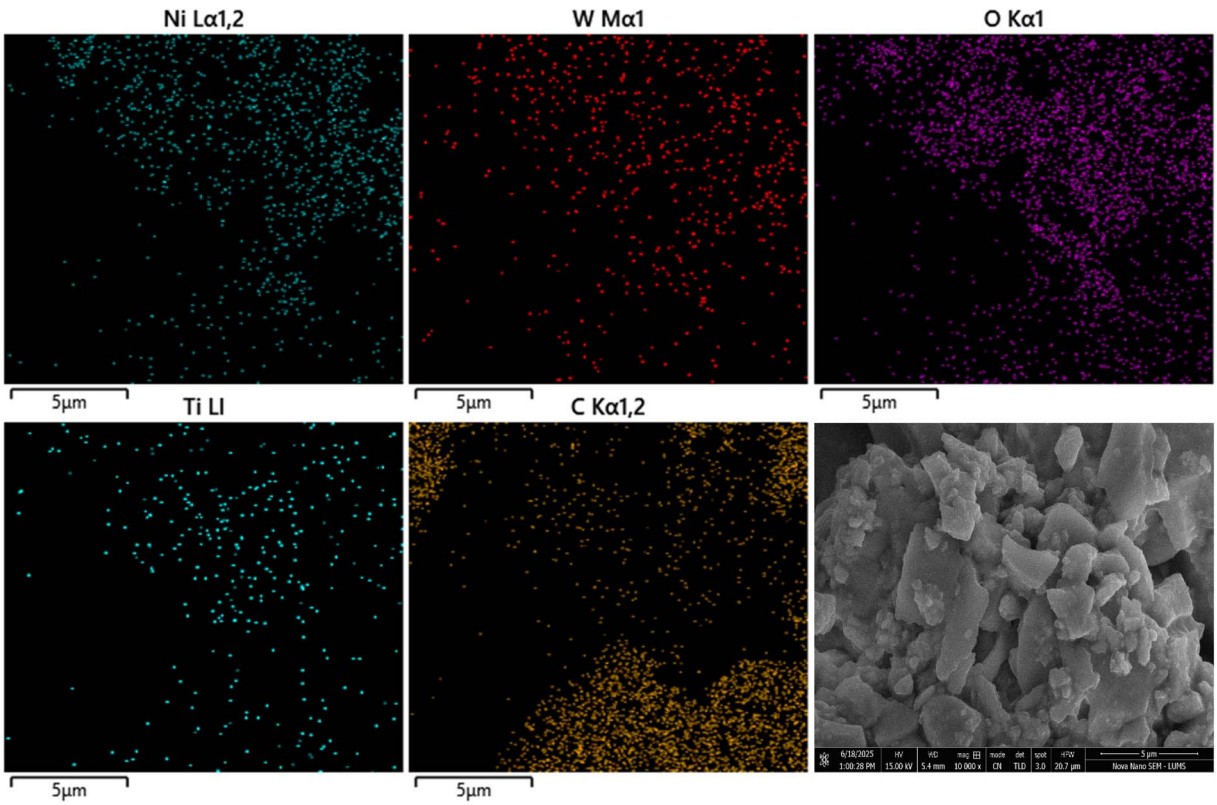

Fig. 5 Elemental mapping of $NiWO_4$/MXene.

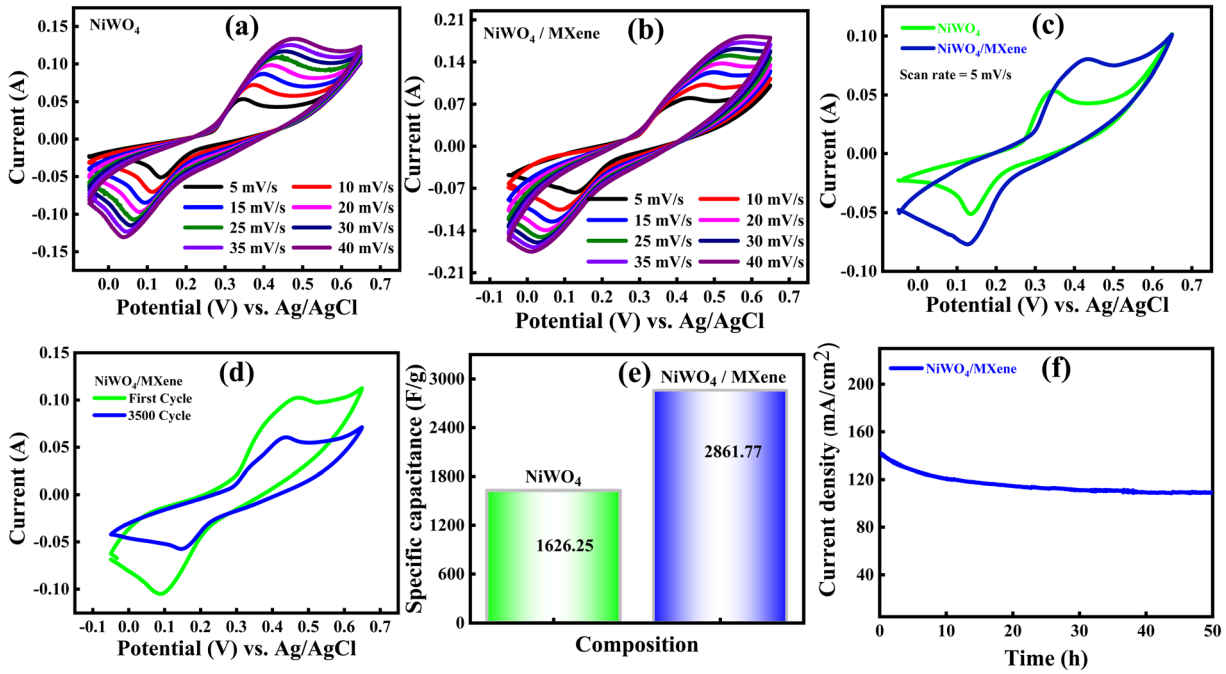

Fig. 6 (a) CV curves of $NiWO_4$, (b) CV curves for $NiWO_4$/MXene at different scan rates, (c) CV curves both samples at 5 mV s^{-1}, (d) CV curves of $NiWO_4$/MXene before and after 3500 cycles, (e) specific capacitance of both samples at 5 mV s^{-1}, and (f) chronoamperometric stability of $NiWO_4$/MXene.

valuable insight into the material's electrochemical properties, making CV an essential tool for assessing electrochemical performance. In Fig. 6(a) and (b), all graphs display clear oxidation and reduction peaks, confirming the faradic nature of the peaks. The curves of pure $NiWO_4$ and $NiWO_4$/MXene at fixed potential windows and various scan rates exhibit two distinct peaks in the positive and negative current regions: cathodic peaks, where reduction occurs, and anodic peaks, where oxidation takes place.[35] The specific capacitance calculated from the CV curves is shown in Table 2.

In Fig. 6(c), the $NiWO_4$/MXene composite shows a larger area under the cyclic voltammetry curves at 5 mV s^{-1}, indicating higher charge storage capacity and C_{sp}, thanks to MXene's incorporation, which increases surface area and provides more active sites for electrochemical reactions. MXene's 2D structure and high conductivity enhance ion diffusion, boost electrochemically active surface area, and improve charge transfer kinetics. Fig. 6(d) shows CV curves of the $NiWO_4$/MXene composite recorded at the 1st and 3500th cycles. The curves' shapes remain consistent, confirming the electrode's excellent long-term stability. As a result, the $NiWO_4$/MXene composite maintains structural integrity and ensures consistent electrochemical behavior over extended periods, making it suitable for long-term energy storage applications. Fig. 6(e) presents a bar graph clearly showing that the composite material has a higher C_{sp}. The C_{sp} values for the $NiWO_4$ and $NiWO_4$/MXene nanocomposite are 1626.25 and 2861.77 F g^{-1}, respectively. These results were calculated using eqn (1) at 5 mV s^{-1}. Chronoamperometry, as shown in Fig. 6(f), revealed that the $NiWO_4$/MXene electrode experienced only a 10% decrease in current density over time, demonstrating outstanding electrochemical stability. The current response remained nearly steady

Table 2 Specific capacitance and area under the CV curve at different scan rates for $NiWO_4$ and $NiWO_4$/MXene

Scan rate (mV s^{-1})	Area under the curve	Specific capacitance (F g^{-1}) of $NiWO_4$	Area under the curve	Specific capacitance (F g^{-1}) of $NiWO_4$/MXene
5	0.016	1626.25	0.028	2861.77
10	0.023	1199.68	0.038	1905.73
15	0.030	1006.31	0.042	1423.31
20	0.035	881.3055	0.046	1162.38
25	0.039	792.0132	0.049	983.88
30	0.042	713.5085	0.050	843.74
35	0.045	655.2731	0.051	739.41
40	0.048	609.8117	0.052	659.72

Table 3 Specific capacitance, energy density, and power density at different current densities

Sample	Current density (A g^{-1})	Discharge time (s)	Specific capacitance (F g^{-1})	Energy density (Wh kg^{-1})	Power density (W kg^{-1})
$NiWO_4$	1.5	264.3	792.90	55.06	750
	1.6	49.80	159.36	11.06	800
	1.7	20.43	69.46	4.82	850
$NiWO_4$@MXene	1.5	515.14	1545.42	107.32	750
	1.6	80.82	258.62	17.96	800
	1.7	33.79	114.88	7.97	850

for 50 hours, showing the electrode's ability to maintain long-term performance. This remarkable stability is attributed to intense interfacial contact and synergistic interaction between $NiWO_4$ and highly conductive MXene layers. MXene offers a durable, conductive framework that facilitates rapid electron transport and helps mitigate volume changes during redox reactions, thereby preventing structural decay of the active material. The specific capacitance, energy density, and power density values at various current densities are summarized in Table 3.

Mathematical equations have been used to determine the capacitive and diffusive contributions for each sample at various scan rates. At this point, determining the *b* and *k* values is crucial, as shown in Fig. 7(a–d) after linear fitting. The contribution graphs after substituting these parameters are displayed in Fig. 7(e and f) for $NiWO_4$ and $NiWO_4$/MXene at different scan rates. It can be observed that the gradual increase in capacitive processes is due to most ions being able to access redox-active sites only at the electrode surface. In contrast, diffusion-controlled mechanisms involve ions penetrating deeper into the electrode. This is how Dunn's model helps explore and discuss the charge-storage mechanism across different materials at varying scan rates.

Additionally, GCD profiles of $NiWO_4$ and $NiWO_4$/MXene electrodes (Fig. 8(a and b)) show distinct, broad plateau regions, especially at lower current densities, indicating strong faradaic redox processes. These plateaus mirror faradaic activity from reversible redox reactions between Ni^{2+}/Ni^{3+} and W^{6+}/W^{5+} couples, confirming capacitive behavior. Fig. 8(a) and (b) display GCD curves for pristine $NiWO_4$ and the $NiWO_4$/MXene composite at different current densities (1, 2, and 3 A g^{-1}), showing a clear trend where the discharge time significantly decreases as the current density increases. This happens because higher currents restrict ion movement and reactions, reducing the material's efficiency. Based on the C_{sp} data in Fig. 8(c), the $NiWO_4$/MXene composite shows significantly higher capacitance across all tested current densities compared to pure $NiWO_4$, reaching a C_{sp} of 1545.42 F g^{-1} at 1.5 A g^{-1}, almost double the 792.90 F g^{-1} for $NiWO_4$. In GCD, C_{sp} is calculated using eqn (2). The composite maintains a high value of approximately 114.88 F g^{-1} even at 1.7 A g^{-1}, indicating improved rate performance, likely due to enhanced conductivity

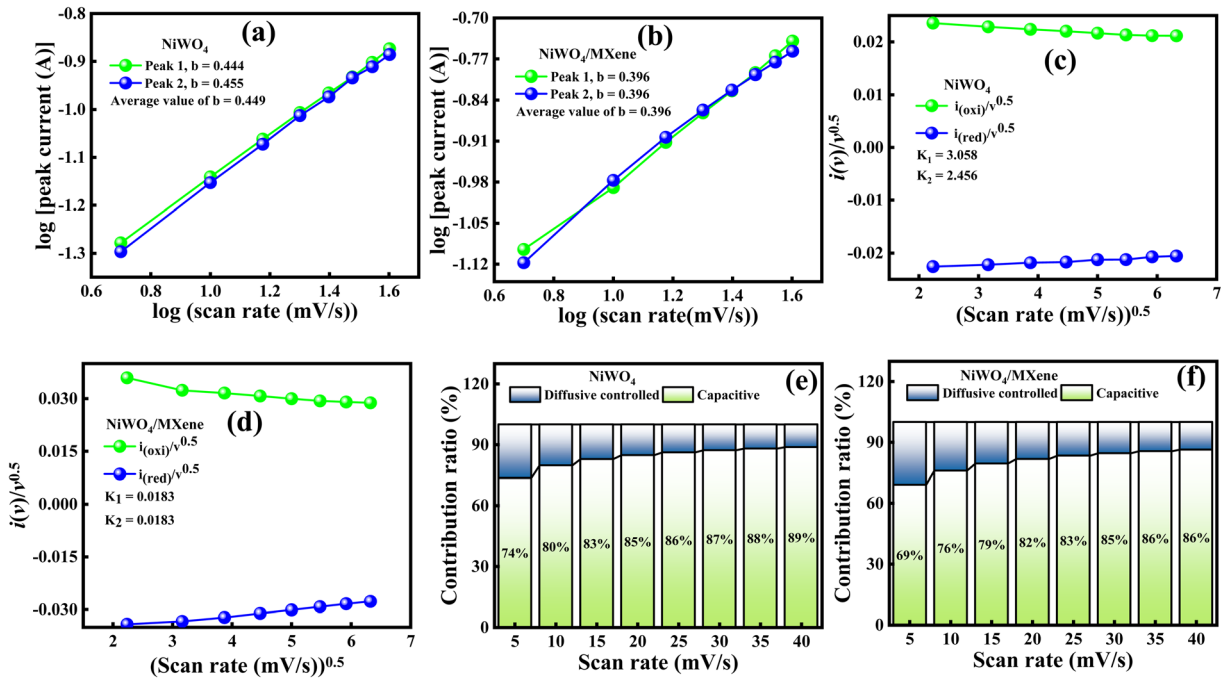

Fig. 7 (a and b) Linear fitting for *b* value, (c and d) graphs for k_1 and k_2, and (e and f) contribution graphs for both samples.

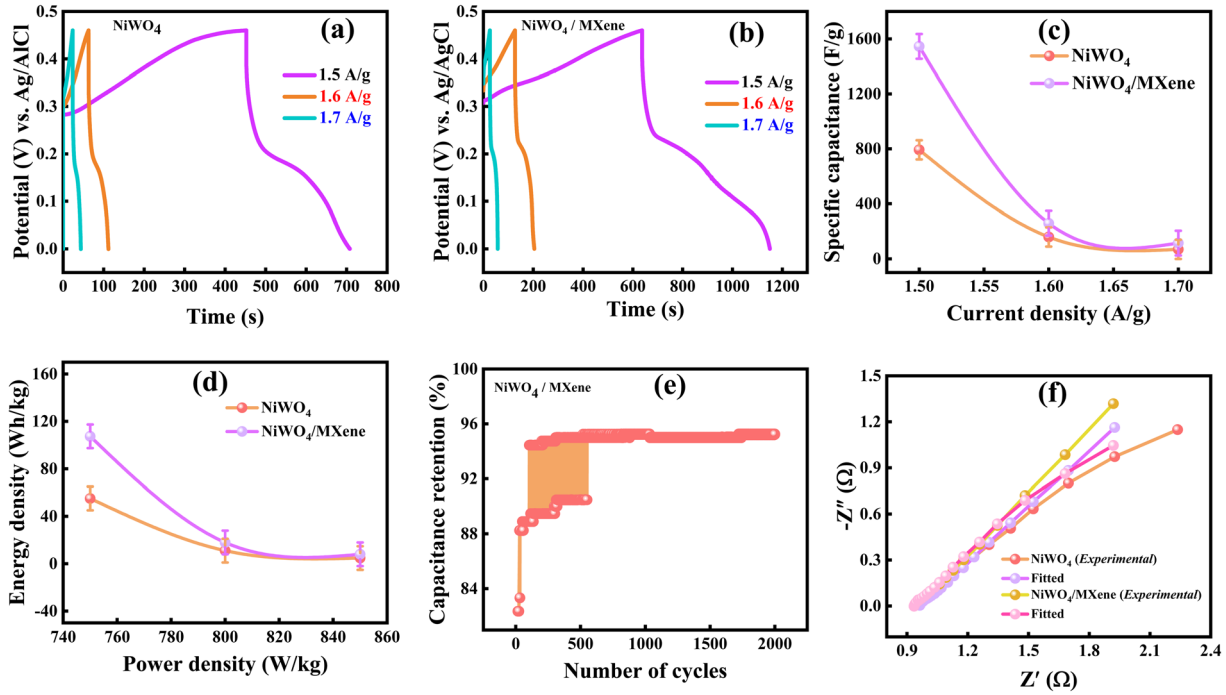

Fig. 8 (a) GCD profiles of $NiWO_4$, (b) $NiWO_4$/MXene, (c) current density *vs.* specific capacitance, (d) Ragone plot, (e) stability test, (f) EIS spectra of both samples after fitting by EC Lab Software.

and ion transport provided by the MXene matrix. This superior electrochemical performance results from the synergy between $NiWO_4$ and MXene, in which the 2D MXene structure greatly enhances electrical conductivity and creates an environment conducive to charge transfer and electrolyte ion mobility. The electrochemical performance parameters of the various reported electrode materials are compared in Table 4.

In a nutshell, the trend of C_{sp} with respect to each current density is shown in Fig. 8(c). In the meantime, the Ragone plot (Fig. 8(d)) shows the ED and PD characteristics of both electrodes, with the $NiWO_4$/MXene composite achieving an impressive ED of 107.32 Wh kg^{-1} at a PD of 750 W kg^{-1}, calculated using eqn (3) and (4), outperforming pure $NiWO_4$. The electrode material exhibits excellent energy storage capabilities, retaining 95.80% after 2000 cycles of charging/discharging, as shown in Fig. 8(e).

Furthermore, EIS is an informative method for assessing key electrochemical characteristics, playing a vital role in understanding the behavior of energy storage materials. Nyquist plots of $NiWO_4$ and $NiWO_4$/MXene electrodes obtained over a frequency range of 0.001–100000 Hz are shown in Fig. 8(f). A point where the impedance curve intersects the *x*-axis indicates electrolyte resistance (R_s), representing the impedance at the electrode–electrolyte boundary. The semicircular arc in the high-frequency region is attributed to charge transfer resistance (R_{ct}), reflecting the ease of electron transfer at the electrode surface. EIS analysis revealed that the R_s values for $NiWO_4$ and $NiWO_4$/MXene were 0.96 Ω and 0.93 Ω, respectively, while the R_{ct} values were 0.13 Ω and 0.09 Ω, respectively. The significant decrease in both R_s and R_{ct} in the $NiWO_4$/MXene composite indicates improved electrical conductivity and faster charge transfer kinetics compared to pristine $NiWO_4$. This enhancement is mainly due to the incorporation of MXene nanosheets, which are known for their large surface area and high electrical conductivity. These properties create efficient electron pathways and facilitate rapid charge transport across

Table 4 Performance parameters of different electrode materials

Material	Specific capacitance ($F\ g^{-1}$)	Energy density ($Wh\ kg^{-1}$)	Power density ($W\ kg^{-1}$)	Ref.
$NiWO_4/CoWO_4$	196.70C g^{-1}	30.10	200	1
$NiCoSe_4/NiWO_4$	828.73	—	—	2
$Ni(OH)_2$/Ni-MOF	854	—	—	3
Ni $(OH)_2/Ti_3C_2T_x$	675	9.25	3.2 k	4
$Ti_3C_2T_x$/Ni-MOF	139	19.40	331.8	5
rGO-$NiWO_4$	779	33.50	12.37 k	6
$NiCo_2O_4/NiWO_4$/Ni foam	1178	60.50	850	7
$NiWO_4$/MXene	1545.42	107.32	750	Our work

the electrode–electrolyte boundary. Additionally, MXene provides a conductive framework that reduces internal resistance by enhancing interfacial interactions between the electrolyte and the active material.[36] The $NiWO_4$/MXene electrode displayed a steeper slope in the low-frequency domain, indicating improved ion diffusion.

4. Ion transport properties

4.1. Ionic conductivity

Ionic conductivity is the inherent ability of an electrode material to promote ion diffusion during electrochemical transitions and redox reactions. This property directly influences the electrochemical performance of SC devices. Materials that exhibit better charge–discharge behavior and higher PD have high ionic conductivity, enabling faster ion movement and more efficient redox reactions. eqn (5) is used to calculate ionic conductivity, enabling an accurate assessment of the material's ion transport properties.[31]

$$\sigma = \frac{L}{R_i \times A} \tag{5}$$

where R_i is the ionic resistance, which indicates the solution resistance (R_s) calculated from EIS data, while L, A, and σ represent the thickness of the electrode, the cross-sectional area of the electrode, and the ionic conductivity. At this instant, the ionic conductivity is quantitatively estimated to be 0.093 and 0.096 S cm^{-1}.

4.2. Transference number

The transference number is the percentage of current carried by cations and anions in an electrolyte, which is vital in SCs and batteries and highlights their role in ionic conduction. Several factors influence ionic conduction, including ionic size, ion mobility, association or dissociation, polarization effects, solvent viscosity, and temperature. Mobility also depends on ionic size, with smaller ions generally moving faster. Increased polarization or internal resistance between the electrode and electrolyte can slow down ion movement. The transference number ranges from 0 to 1. To enhance ion-selective transport in SCs or batteries, understanding ion transport kinetics and the transference number is essential. Sorenson and Jacobsen's eqn (6) is used to calculate the transference number.[32]

$$t_+ = \frac{1}{1 + Z_d(0)/R_b} \tag{6}$$

In this equation, t_+ represents the cation transference number, and we can calculate t_-, the anion transference number, through the relation ($t_- = 1 - t_+$), while $Z_d(0)$ is the Warburg resistance, and R_b demonstrates the electrolyte resistance. Using the above relationship, the cation contribution for $NiWO_4$ is 0.26, whereas it is 0.36 for $NiWO_4$/MXene. This suggests a greater cationic contribution in the $NiWO_4$/MXene composite compared to pure $NiWO_4$. A comparison of ion transport properties of different materials is presented in Table 5.

4.3. Rate constant

The rate constant indicates the speed of a reaction and provides detailed information on how quickly electrons transfer between the electrode and electrolyte ions during a redox reaction. It is a kinetic parameter closely related to charge-transfer resistance. A high rate constant indicates a fast redox reaction, resulting in greater charge storage, higher power, and improved performance. The rate constant is calculated using the equation eqn (7) provided.[33]

$$\text{Rate constant} = \frac{RT}{F^2 \times R_{ct} \times C} \tag{7}$$

Here, R and T in the numerator represent the universal gas constant and room temperature, respectively. At the same time, parameters in the denominator, such as F, R_{ct}, and C, are correspondingly linked to the Faraday constant, the charge transfer resistance calculated from EIS analysis, and the electrolyte concentration. Within this perspective, the rate constant for $NiWO_4$ and $NiWO_4$/MXene is estimated to be 2.96×10^{-7} and 2.86×10^{-7}, respectively.

4.4. Exchange current density

Exchange current density is a crucial parameter in electrochemistry, measuring the rate of charge transfer reactions at the electrode–electrolyte interface when no current flows. It is the rate at which electrons are exchanged between the electrode and ions in the electrolyte when the electrode is at the equilibrium potential. A high exchange current density indicates fast reaction kinetics and a lower overpotential required to drive current. This can be assessed using eqn (8).[33]

Table 5 Comparison table of ion transport attributes of different materials

Sample	Ionic conductivity (S cm^{-1})	Transference number (t_+)	Rate constant (cm s^{-1})	Exchange current density (A g^{-1})	Diffusion coefficient (m^2 s^{-1})	Ref.
$LaNiO_3$/MXene	6.3×10^{-3}	0.3	—	—	9.5×10^{-13}	30
$BiMnO_3$/CNTs	0.978×10^{-3}	0.31	3.91×10^{-7}	—	3.45×10^{-18}	31
ZnO/CNTs	0.046	0.01	6.49×10^{-7}	—	3.69×10^{-12}	32
MoS_2/Se/CNTs	16.0×10^{-3}	0.35	0.0029	0.74	—	33
$BaCoO_3$/rGO	0.128	0.2	—	—	4.51×10^{-13}	34
$NiMnO_3$/CNTs	0.78×10^{-3}	0.61	—	—	—	35
$NiWO_4$/MXene	0.037	0.36	2.86×10^{-7}	0.014	1.26×10^{-14}	This work

$$J_0 = \frac{RT}{n \times F \times R_{ct}} \quad (8)$$

By employing this relationship, the values of the rate constant are computed to be 2.96×10^{-7} and 2.86×10^{-7} cm s^{-1} for $NiWO_4$ and $NiWO_4$@MXene.

4.5. Cation mobility

It is another transport property that explains how positive ions (cations) move readily in an electrolyte when a potential is applied. Fast cation mobility indicates how easily ions can move and store charge, leading to high power density. This property varies between different electrolytes and systems, with KOH and NaOH being the most common due to their low cost, minimal adverse effects, and anti-corrosive properties. Cations are preferred because of their lower solvent-shell energy and their greater ease of diffusion in an electrolyte. In this context, cation mobility in KOH is described by eqn (9).[33]

$$u_+ = \frac{t_+ \times \sigma}{n \times z^2 \times e} \quad (9)$$

In the above equation, t_+ and σ are the transference number of the cation and ionic conductivity, respectively. The parameters n, Z^2, and e represent the number density, charge number, and elementary charge, respectively. Using this standard relationship, the cation mobilities for $NiWO_4$ and $NiWO_4$/MXene are 1.93×10^{-8} and 2.99×10^{-8} m^2 V^{-1} s^{-1}, respectively. The superior cationic mobility significantly accelerates charge transport within the electrolyte, ensuring swift ion dynamics at the electrode interface. This enhanced mobility directly translates into higher PD and exceptional rate capability in SC systems.

4.6. Diffusion coefficient

To understand the electrochemical performance of energy storage devices, it is essential to measure ion diffusion. By evaluating the diffusion coefficient, the ion-exchange reaction at the electrode–electrolyte interface can be readily estimated. A high diffusion coefficient indicates a high-rate capability and greater ion movement, leading to a large storage capacity. The diffusion coefficient is determined from the following equation eqn (10).[31]

$$D^{EIS}/K^+ = \frac{R^2T^2}{2 \times A^2 \times n^4 \times F^4 \times c^2 \times \delta^2} \quad (10)$$

Eqn (10) demonstrates the diffusion of potassium ions (K^+) in a KOH electrolyte, where parameters, such as R, T, A, n, F, c, and δ are the gas constant, temperature, electrode surface area, electrons, Faraday constant, concentration of electrolyte, and Warburg coefficient, respectively. The values of the diffusion coefficient for $NiWO_4$ and $NiWO_4$/MXene are determined to be 6.57×10^{-15} and 1.26×10^{-14} m^2 s^{-1}.

The value of C has been calculated using the Nernst equation, as presented in eqn (11).[32]

$$E = E^0 + \frac{RT}{nF}\ln\frac{C_{surface}}{C_{bulk}} \quad (11)$$

The most general and extended form of the Nernst equation (eqn (12)) is given below,

$$C_{surface} = C_{bulk} \times e^{\left(\frac{nF\left(E-E^\circ\right)}{RT}\right)} \quad (12)$$

Here, $C_{surafce}$ indicates electrolyte type concentration at the electrode surface, but C_{bulk} refers to the total number of ions in solution concentration.

5. Conclusion

In this study, high-performance $NiWO_4$/MXene composite electrodes were successfully synthesized *via* a hydrothermal method and systematically evaluated for their suitability in advanced SC applications. The composite demonstrated remarkable specific capacitance values of 2861.77 F g^{-1} (CV at 5 mV s^{-1}) and 1545.42 F g^{-1} (GCD at 1.5 A g^{-1}), along with excellent rate capability and minimal internal resistance (R_s = 0.93 Ω, R_{ct} = 0.09 Ω), confirming highly efficient charge storage and rapid redox kinetics. Importantly, the investigation into ion transport dynamics and cation mobility revealed accelerated ionic diffusion and enhanced ion–electron coupling, which strongly contributed to the superior performance. These improvements are attributed to the synergistic interaction between $NiWO_4$ and MXene, offering abundant electroactive sites, increased conductivity, and fast ion-transport pathways. Overall, this work provides new insight into the fundamental transport mechanisms governing high-efficiency electrode materials, positioning $NiWO_4$/MXene as a promising candidate for next-generation, fast-charging energy storage technologies. Future studies may explore device-level integration, long-term operational stability under practical conditions, and optimization of composite ratios or scalable fabrication routes to further advance their application in commercial SCs.

Conflicts of interest

The authors declare that they have no known competing financial interests or personal relationships that could have appeared to influence the work reported in this paper.

Data availability

Data will be made available on request.

Funding

The authors extend their appreciation to the Deanship of Research and Graduate Studies at King Khalid University for funding this work through Large Research Project under grant number RGP2/35/46.

Acknowledgements

The authors extend their appreciation to the Deanship of Research and Graduate Studies at King Khalid University for funding this work through Large Research Project under grant number RGP2/35/46.

References

1 Y. Wang, *et al.*, High rate capability of mesoporous $NiWO_4$–$CoWO_4$ nanocomposite as a positive material for hybrid supercapacitor, *Mater. Chem. Phys.*, 2016, **182**, 394–401.
2 S. Aftab, *et al.*, Fabrication of $NiCo_2Se_4$@ $NiWO_4$ nanocomposites for high performance supercapacitor applications, *J. Energy Storage*, 2022, **56**, 106111.
3 S. Rajkumar, *et al.*, Investigation on $NiWO_4$/PANI composite as an electrode material for energy storage devices, *New J. Chem.*, 2021, **45**, 20612–20623.
4 P. Lokhande, *et al.*, 2D MXene incorporated nickel hydroxide composite for supercapacitor application, *J. Mater. Sci.: Mater. Electron.*, 2024, **35**, 697.
5 Shavita, *et al.*, Exploring MXene-MOF composite for supercapacitor application, *Mater. Chem. Phys.*, 2024, **322**, 129463.
6 D. J. Patil, *et al.*, Facial synthesis of reduced graphene oxide – amorphous nickel tungstate composite for flexible hybrid asymmetric solid state supercapacitor application, *J. Energy Storage*, 2023, **72**, 108729.
7 M. Dayanithy, *et al.*, Synergistic integration of $NiCo_2O_4$ and $NiWO_4$ nanosheets on Ni foam for advanced supercapacitor applications, *J. Porous Mater.*, 2025, 1–11.
8 K. Xue, *et al.*, Di-imidazolium ionic liquid based electrolytes for high voltage electrochemical double layer capacitors, *J. Energy Storage*, 2024, **83**, 110473.
9 P. Bhojane, Recent advances and fundamentals of Pseudocapacitors: Materials, mechanism, and its understanding, *J. Energy Storage*, 2022, **45**, 103654.
10 B. G. S. Raj, *et al.*, One-pot sonochemical synthesis of hierarchical $MnWO_4$ microflowers as effective electrodes in neutral electrolyte for high performance asymmetric supercapacitors, *Int. J. Hydrogen Energy*, 2019, **44**(21), 10838–10851.
11 H. Matsui, *et al.*, The electronic behaviors of visible light sensitive Nb_2O_5/Cr_2O_3/carbon clusters composite materials, *Curr. Appl. Phys.*, 2009, **9**(3), 592–597.
12 S. J. Patil, *et al.*, Bottom-up Approach for Designing Cobalt Tungstate Nanospheres through Sulfur Amendment for High-Performance Hybrid Supercapacitors, *ChemSusChem*, 2021, **14**(6), 1602–1611.
13 S. S. Patil, *et al.*, Hierarchical hydrothermal synthesis monoclinic $NiWO_4$ nanosphere material for high-performance energy storage application, *J. Energy Storage*, 2024, **100**, 113394.
14 A. Gouveia, *et al.*, Electronic structure, morphological aspects, and photocatalytic discoloration of three organic dyes with $MgWO_4$ powders synthesized by the complex polymerization method, *J. Inorg. Organomet. Polym. Mater.*, 2020, **30**, 2952–2970.
15 D. J. Patil, *et al.*, Binder-Free Synthesis of Mesoporous Nickel Tungstate for Aqueous Asymmetric Supercapacitor Applications: Effect of Film Thickness, *Energy Technol.*, 2022, **10**(8), 2200295.
16 J. Tian, *et al.*, Solvothermal synthesis of $NiWO_4$ nanostructure and its application as a cathode material for asymmetric supercapacitors, *RSC Adv.*, 2018, **8**(73), 41740–41748.
17 J. M. Gonçalves, *et al.*, Trimetallic oxides/hydroxides as hybrid supercapacitor electrode materials: a review, *J. Mater. Chem. A*, 2020, **8**(21), 10534–10570.
18 J. Tang, *et al.*, Effect of Co^{2+} Doping on Electrochemical Properties of Nickel Metal Tungstate (NiWO4) Positive Material, *Electron. Mater. Lett.*, 2024, **20**(4), 459–473.
19 L. Zhang, *et al.*, Influencing factors on synthesis and properties of MXene: a review, *Processes*, 2022, **10**(9), 1744.
20 N. K. Mishra, *et al.*, Synthesis, Characterizations, and Electrochemical Performances of Highly Porous, Anhydrous $Co_{0.5}Ni_{0.5}C_2O_4$ for Pseudocapacitive Energy Storage Applications, *ACS Omega*, 2022, **7**(2), 1975–1987.
21 J. Tang, *et al.*, Effect of Co^{2+} Doping on Electrochemical Properties of Nickel Metal Tungstate ($NiWO_4$) Positive Material, *Electron. Mater. Lett.*, 2024, **20**(4), 459–473.
22 W. Choi, *et al.*, Dynamics of simultaneous, single ion transport through two-dimensional nanochannels, *J. Am. Chem. Soc.*, 2011, **133**, 14236–14239.
23 A. E. Gerdroodbar, *et al.*, A review on ion transport pathways and coordination in electrolytes, *Mater. Today: Proc.*, 2023, **77**, 1524–1535.
24 Z. Karimi, *et al.*, Ultra-low cost supercapacitors from coal char: effect of electrolyte on double layer capacitance, *Energy Adv.*, 2023, **2**(7), 1036–1044.
25 R. Nie, *et al.*, Pulsed laser deposition of $NiSe_2$ film on carbon nanotubes for high-performance supercapacitor, *Int. J. Eng. Sci.*, 2018, **6**(15), 22–29.
26 T. M. Salama, *et al.*, Synthesis of graphene oxide interspersed in hexagonal WO_3 nanorods for high-efficiency visible-light driven photocatalysis and NH_3 gas sensing, *Front. Chem.*, 2019, **7**, 722.
27 A. Irshad, *et al.*, Probing the synergistic effect of MXene ($Ti_3C_2T_x$) and MWCNTs on $NiWO_4$ for superior water-splitting and supercapacitor studies, *Fuel*, 2025, **392**, 134811.
28 L.-Å. Näslund and I. Persson, XPS spectra curve fittings of $Ti_3C_2T_x$ based on first principles thinking, *Appl. Surf. Sci.*, 2022, **593**, 153442.
29 Z. Zhu, *et al.*, Flexible and lightweight $Ti_3C_2T_x$ MXene@ Pd colloidal nanoclusters paper film as novel H_2 sensor, *J. Hazard. Mater.*, 2020, **399**, 123054.
30 A. Shakoor, *et al.*, Diffusion Dynamics, and Transference Numbers for $LaNiO_3$/MXene Supercapacitor Electrodes, *Batteries Supercaps*, 2025, 2500014.
31 S. Fatima, *et al.*, Microstructural tailoring for enhanced response of carbon nanotube-filled $BiMnO_3$ electrodes, *Mater. Chem. Phys.*, 2025, **345**, 131198.

32 A. Hussain, *et al.*, Synergistically tailored ionic conduction and transport in ZnO/CNTs based electrodes with enhanced electrochemical efficiency in supercapacitors, *Electrochim. Acta*, 2025, **536**, 146736.
33 A. Shehzad, *et al.*, Investigating electrochemical properties in CNT-modified MoS_2/Se composites for supercapacitor electrodes, *Electrochim. Acta*, 2025, **656**, 238067.
34 M. Shehzad, *et al.*, Tuning diffusion coefficient, ionic conductivity, and transference number in rGO/$BaCoO_3$ electrode material for optimized supercapacitor energy storage, *RSC Adv.*, 2025, **15**, 6308–6323.
35 A. Iqbal, *et al.*, Enhanced ionic conductivity in synergistically developed $NiMnO_3$/CNTs nanocomposite electrode material in hybrid capacitors, *Electrochim. Acta*, 2025, **134**, 118207.
36 Y. Ma, *et al.*, Fe_2O_3 Nanoparticles Anchored on the $Ti_3C_2T_x$ MXene Paper for Flexible Supercapacitors with Ultrahigh Volumetric Capacitance, *ACS Appl. Mater. Interfaces*, 2020, **12**, 41410–41418.